ELECTROCATALYSIS

Selective increase in CO_2 electroreduction activity at grain-boundary surface terminations

Ruperto G. Mariano,[1] Kim McKelvey,[2]* Henry S. White,[2] Matthew W. Kanan[1]†

Altering a material's catalytic properties requires identifying structural features that give rise to active surfaces. Grain boundaries create strained regions in polycrystalline materials by stabilizing dislocations and may provide a way to create high-energy surfaces for catalysis that are kinetically trapped. Although grain-boundary density has previously been correlated with catalytic activity for some reactions, direct evidence that grain boundaries create surfaces with enhanced activity is lacking. We used a combination of bulk electrochemical measurements and scanning electrochemical cell microscopy with submicrometer resolution to show that grain-boundary surface terminations in gold electrodes are more active than grain surfaces for electrochemical carbon dioxide (CO_2) reduction to carbon monoxide (CO) but not for the competing hydrogen (H_2) evolution reaction. The catalytic footprint of the grain boundary is commensurate with its dislocation-induced strain field, providing a strategy for broader exploitation of grain-boundary effects in heterogeneous catalysis.

Bulk defects such as grain boundaries (GBs) and dislocations have been used extensively to control properties such as mechanical strength, plasticity, and conductivity (*1*), but relatively little is known about how defects alter catalytic properties. Bulk defects create substantial structural perturbations in their vicinity and are often trapped by large kinetic barriers (*2*), but it is unclear whether bulk defects can create regions of enhanced catalytic activity when they terminate at a surface. We previously proposed that the high densities of GBs present in nanocrystalline "oxide-derived" catalysts were responsible for their improved CO_2-to-CO and CO-to-fuels electrocatalytic activity (*3*–*5*). More recently, we showed quantitative correlations between electrocatalytic activity and GB density for catalysts composed of discrete Au and Cu nanoparticles (NPs) (*6*, *7*). Other recent studies have also reported GB effects on both electrochemical and chemical catalysis with nanostructured materials (*8*–*11*). Although these correlations are consistent with the formation of active regions at GB surface terminations, direct evidence requires spatially resolved measurements. In addition, the use of GBs as catalyst design elements will require an understanding of how activity depends on GB structure. The short length scale of nanostructured catalysts makes it extremely challenging to quantify GB structure distributions and to correspondingly elucidate the structural disorder and unusual reactivity induced in their vicinity.

Here, we investigate GB effects on flat, polycrystalline Au electrodes with large grain sizes, which permit spatial resolution of the GB surface-termination regions (Fig. 1). Using bulk electrochemical measurements, we show that CO_2 reduction activity increased with GB density on these electrodes, but there was no correlation with H_2 evolution activity. By probing the local electrocatalytic activity across GBs using scanning electrochemical cell microscopy (SECCM) (*12*–*15*), we show that the origin of this effect is a selective increase in CO_2 reduction activity at the GB surface terminations. The magnitude of the increase and the width of the region exhibiting increased activity depended on the GB geometry, which determined the concentration of dislocations in the GB region. Our results explicitly link GB-trapped dislocations to catalytic activity.

The density and geometries of GBs in polycrystalline materials with >100 nm grain sizes can be resolved using electron backscatter diffraction (EBSD) in a scanning electron microscope (SEM) (*16*). EBSD is a nondestructive technique in which individual diffraction patterns are obtained from backscattered electrons as an electron beam is rastered across a sample. The diffraction pattern from each spot reveals the orientation of the underlying crystallite, with a penetration depth of ~30 nm in Au (*17*, *18*). The diffraction patterns can be combined to construct an EBSD orientation map, which shows the individual grains and their orientations at the surface of a material and thereby reveals the GB density and geometry (i.e., the misorientation of the neighboring grains at each GB) (*19*).

Using EBSD, we interrogated the grain structure of mirror-smooth, flat polycrystalline Au foil and a series of samples that were annealed at progressively higher temperatures (200°, 500°, 700°, and 970°C) to alter their microstructure (Poly-Au, Ann. 200, Ann. 500, Ann. 700, and Ann. 970). Multiple orientation maps were obtained for each sample to quantitatively compare the grain orientations and GBs. (Representative images are shown in Fig. 2, A to E). The images were used to generate *z*-direction orientation frequency maps showing the distribution of grain orientations for each sample (Fig. 2F). The frequency map of Poly-Au was almost fully populated, indicating that the surface crystallites are randomly oriented. Annealing to higher temperatures progressively decreased the diversity of crystallographic orientation, but no single preferred orientation emerged even at 970°C. This result was corroborated by electrochemically probing the surface faceting of the samples using Pb underpotential deposition (Pb UPD) (fig. S1) [see the supplementary materials for all experimental details (*20*)] (*21*). Integration of the (110) and (111) stripping features in Pb UPD voltammograms yielded no relation between the annealing temperature and the (110)/(111) surface population ratio (table S1). The lack of a dominant orientation after annealing is consistent

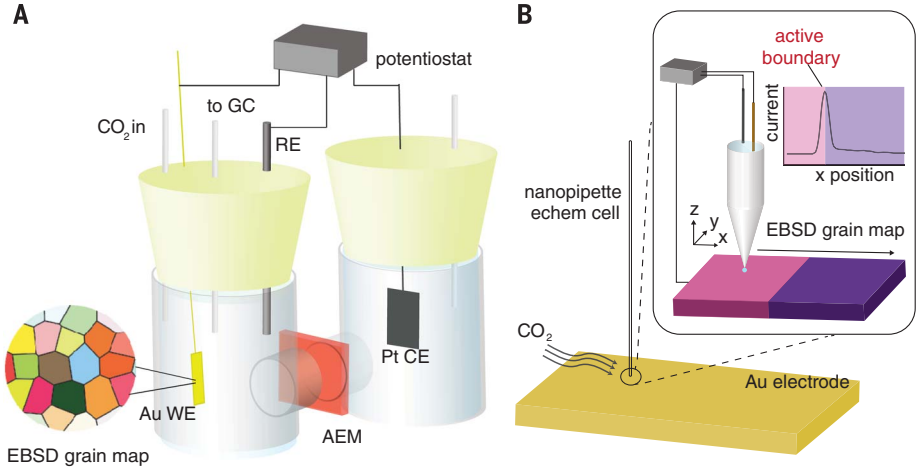

Fig. 1. Two approaches detailed here for electrochemical characterization of defect effects on CO_2 reduction. (**A**) Bulk electrolysis of a well-defined polycrystalline Au electrode within a glass, two-compartment H cell. (**B**) SECCM using a ~300-nm nanopipette electrochemical cell.

[1]Department of Chemistry, Stanford University, 337 Campus Drive, Stanford, CA 94305, USA. [2]Department of Chemistry, University of Utah, 315 S 1400 E, Salt Lake City, UT 84112, USA. *Present address: School of Chemistry, Trinity College Dublin, Dublin 2, Ireland.
†Corresponding author. Email: mkanan@stanford.edu

with previous x-ray diffraction and EBSD studies of annealed Au (*22*).

The total GB density and distribution of GB geometries for each of the samples were calculated from the EBSD maps. In the unannealed Poly-Au sample, the ~1-μm grains were separated by GBs with a large diversity in structure: ~20% of the GBs met the criterion of a coincident site lattice (CSL) boundary (*16*), whereas ~80% of the GBs were non-CSL boundaries. Of the CSL boundaries, most were Σ3 (68%) (also known as twin boundaries), and a minor fraction (2.4%) were Σ9. The non-CSL boundaries included a large proportion of boundaries between grains with a small degree of misorientation (i.e., low-angle GBs). Annealing increased the grain size substantially (Fig. 2, B to E). The overall GB density declined as the annealing temperature was increased. The majority of the GBs after annealing were Σ3, with smaller amounts of Σ9 and non-CSL GBs. The combined proportion of other CSL GB types, such as Σ5<100> and GBs with Σ > 9, were reduced to less than 5% of the overall GB surface population. Total GB densities and GB densities of individual structures are summarized in table S1.

The electrochemical activity of the electrodes was evaluated by performing bulk electrolyses at −0.4 V versus the reversible hydrogen electrode (RHE) in 0.5 M $NaHCO_3$ under 1 atm of CO_2 in a two-compartment H cell (Fig. 1A). A relatively low overpotential for the CO_2-to-CO reduction reaction was selected to minimize the activity from ordinary Au surface facets so that GB effects could be easily quantified. The products of electrolysis, CO and H_2, were quantified by gas chromatography (GC) to determine their partial current densities. Integration of the Cu UPD stripping wave in cyclic voltammograms indicated that the electrodes were all flat (roughness factors very near 1.0) (table S2). Highly reproducible measurements were obtained for these low surface area electrodes by taking precautions to eliminate electrolyte impurities (*20*, *23*).

The surface area–normalized current density for CO_2 reduction to CO (j_{CO}) decreased monotonically as the temperature of the annealing pretreatment was increased (Fig. 2 and fig. S2.) Because the electrodes are flat, these differences were not a consequence of differences in local pH or mass transport effects caused by rough morphologies (*24*). Additionally, no correlation was evident between j_{CO} and the (110)/(111) plane population ratio obtained by Pb UPD (table S1), indicating that surface faceting did not substantially affect CO_2 reduction activity. EBSD analysis of a Au electrode before and after extended electrolysis showed no difference in the density and geometry of GBs (fig. S3).

The stability of the GBs under electrolysis conditions permitted assessment of GB effects on activity by comparing steady-state current densities to GB geometry densities obtained by EBSD. A monotonic increase in j_{CO} was observed with the total GB density of the electrodes (Fig. 2G). The activity of Poly-Au was lower than what would be expected from the trend in the other four samples, which suggested that the GB effect saturated (see below). When compared with specific GB geometries, j_{CO} showed a strong positive linear correlation with the density of both Σ3 and Σ9 GBs (fig. S4). In sharp contrast, the total GB density, Σ3 GB density, and Σ9 GB density all showed no correlation to the surface area–normalized current density for the competing H_2O reduction to H_2 (j_{H2}). These results mirror what we observed previously with Au NP catalysts (*6*), but here we have eliminated any possible convoluting effects of nanoscale morphology changes.

The presence of a strong GB-activity correlation on flat Au electrodes provided a system for testing enhanced activity at GB surface terminations directly with SECCM. This electrochemical scanning probe technique uses a nanoscale droplet situated at the end of a nanopipette to confine measurements to only the portion of the surface in contact with the droplet. Previous applications of SECCM for catalysis have investigated O_2 reduction and hydrazine oxidation on polycrystalline Pt electrodes (*25*, *26*). These studies revealed facet-dependent catalytic activity but did not observe GB effects for these reactions.

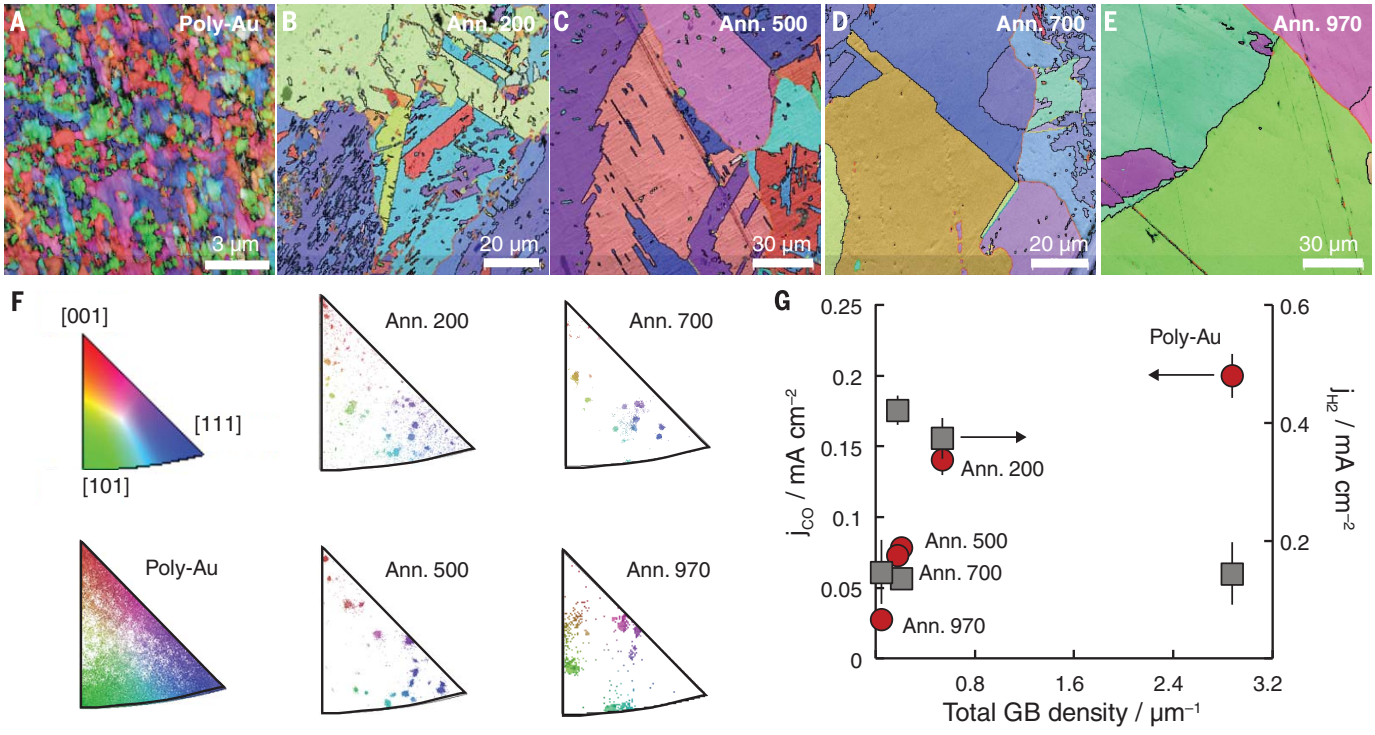

Fig. 2. Bulk electrochemical and grain-boundary density characterization of polycrystalline Au electrodes. (**A** to **E**) Representative EBSD maps of electrodes used to generate GB geometry-activity correlations. Each pixel is a single diffraction pattern, and each color corresponds to a unique orientation. (**F**) Legend showing pole figure orientations and orientation frequency maps for each of the samples. Each pixel in the orientation frequency maps corresponds to a pixel in each map in (A) to (E), showing the distribution of orientations measured by EBSD. (**G**) j_{CO} and j_{H2} versus total GB density for the five Au samples. Values are the average of triplicate measurements of activity; error bars indicate mean ± SD. j_{CO} and j_{H2} refer to the surface area–normalized values, which are close to the geometric current densities because of the low roughness values.

To maintain a constant tip-substrate distance, SECCM typically uses a dual-barrel pipette probe containing two quasi-reference/counter electrodes to generate a feedback signal as the nanoelectrochemical cell is scanned across a sample surface by using piezoelectric motors, as in atomic force microscopy. We initially attempted to use this configuration but found that the quasi-reference/counter electrodes led to transient potential drift and metal deposition on the Au substrates when used in Cl^--free electrolyte at the potentials required for CO_2 reduction. We therefore switched to using a single-barrel pipette probe operated in "hopping mode" with a traditional three-electrode potentiostat (*20*). The probe contains electrolyte, a Au counter electrode, and a Ag/AgCl leakless reference electrode (Fig. 1B). Holding the Au substrate at a fixed potential versus the Ag/AgCl reference within the nanoelectrochemical cell, current flows when the droplet at the end of the probe makes contact with the Au surface. The current is recorded for a specified time interval, and the probe is then retracted to break the droplet/surface contact, translated laterally, and then lowered to the Au surface for the subsequent measurement (fig. S5). The combination of these measurements allows the construction of line scans or maps across regions of interest. The topography is recorded by the vertical distance required to make contact at each hop.

A sample for SECCM imaging was prepared by cleaving a 500-μm-diameter Au wire and annealing it at 970°C to create a coarse-grained cross section in which the GBs can be optically located. EBSD imaging showed ~200-μm grains and a 17° GB between two grains with mixed (100)/(111) orientation (Fig. 3A). The GB was located optically before the SECCM scans, because the GB is associated with a ~0.5-μm indentation in the surface, which is commonly observed in coarse-grained samples annealed at high temperatures (fig. S6) (*27*). A pipette probe with a ~300-nm aperture was used for the SECCM to afford submicrometer spatial resolution.

Hopping-mode current profiles with 500-nm step size were obtained across the GB surface termination at –0.99 V versus Ag/AgCl in 10 mM $KHCO_3$ separately under Ar and CO_2 to assess the differences under H_2O reduction and CO_2 reduction conditions (fig. S5 for experimental schematic). Under Ar, a step in current was observed from one grain to the neighboring grain (Fig. 3B), which indicated a difference in the H_2 evolution activity between the two grain surfaces. This difference may reflect a difference in the abundance of (111) facets on the two grains (*28*), although the grain orientation determined by EBSD does not directly reveal the surface faceting. When the probe was rastered back and forth across the GB to generate an electrocatalytic heat map, we observed approximately two regions of activity, and there was no localized enhancement at the GB (Fig. 3D).

In contrast, when SECCM was performed under CO_2 at the same potential versus Ag/AgCl, the two grains displayed similar currents, but the GB region showed a peak that was 2 to 2.5 times as large as the neighboring grains (Fig. 3C). The overall current was lower under CO_2 compared with Ar, which is consistent with a suppression of H_2 evolution in the presence of CO_2 (*6*, *29*). When the probe was rastered back and forth across the GB to generate an electrocatalytic heat map, the GB region consistently showed increased activity relative to the surrounding grain surfaces (Fig. 3E). The increase was seen in the three or four steps across the GB that span ~2 μm, which implied that the GB surface termination perturbed the surface structure with a footprint that was at least this wide. The current increases are unlikely the result of an increase in the droplet size caused by the shallow surface indentation in the GB region (fig. S6) because no GB-localized enhancement was observed in the Ar current

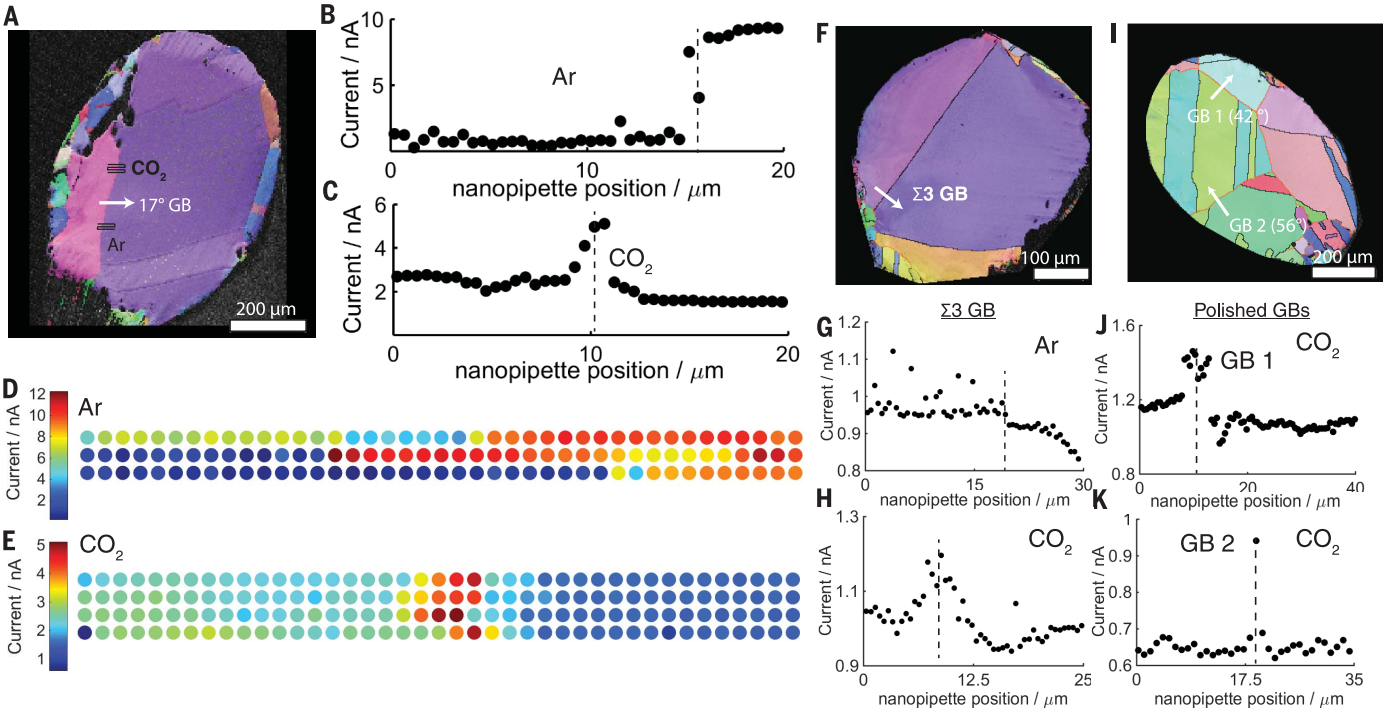

Fig. 3. Scanning electrochemical cell microscopy of CO_2 and H_2O reduction on Au. (**A**) EBSD orientation map of sample used for (B) to (E). Inset text and paths indicate location where line scans and maps were collected. (**B**) Line scan generated from individual constant potential electrolysis across the GB under 1 atm Ar. (**C**) Line scan under 1 atm CO_2. Dashed lines indicate location of GBs inferred from optical images and topography data. (**D**) Electrocatalytic heat map composed of multiple line scans across the GB under 1 atm Ar. (**E**) Heat map under 1 atm CO_2. Each 500-nm dot represents a landing point for the nanopipette cell, and each horizontal line is a single line scan analogous to (B) and (C). Measurements shown in (B) to (E) were performed with the same nanopipette tip. (**F**) EBSD orientation map of sample used for (G) and (H). (**G**) Line scan obtained across the GB in (F) under 1 atm Ar. (**H**) Line scan obtained across the same GB under 1 atm CO_2. The same nanopipette was used for (G) and (H). (**I**) EBSD orientation map of an Ar ion-milled sample with minimal surface topography. (**J**) Line scan obtained under CO_2 across the boundary marked GB1 in (I). (**K**) Line scan obtained across the boundary marked GB2. Separate nanopipettes were used for (J) and (K).

profiles. The peak at the GB region in the activity map under CO_2, in contrast with the step observed under Ar, indicates that the GB surface termination selectively increased CO_2 reduction catalysis without increasing H_2 evolution.

The activity at a GB surface termination is expected to depend on the GB geometry because the geometry determines the energy and local structure of the GB. To probe the activity of a different GB geometry, we performed SECCM on another sample that has a large Σ3 GB (Fig. 3F). The topography for this GB was very similar to the topography for the 17° GB (fig. S7). The current profile under Ar showed a small step at the GB, indicating a slight difference in the H_2 evolution activity across the two grains (Fig. 3G). In contrast, under CO_2, a peak was again observed in the GB region. The current increase was only 10 to 20% but extended over ~4 μm (Fig. 3H). The smaller magnitude of the effect at this Σ3 GB compared with the increase by a factor of 2 to 2.5 that was seen with the 17° GB in Fig. 3A indicates that this Σ3 GB has a smaller structural effect on the surrounding lattice (see below).

To minimize surface topography, a third sample was prepared in which the surface was polished by Ar ion beam milling after the annealing procedure. The GBs of this sample had very mild or no associated surface indentations (fig. S8). Line scans were performed over two GBs under CO_2 (Fig. 3I). For a 42° GB ("GB 1"), a ~20% current increase was observed over a ~3 μm width (Fig. 3J), whereas a 54° GB (GB 2) showed a ~50% increase at a single step (Fig. 3K).

The currents observed in the SECCM measurements correspond to large current densities (assuming a contact radius of 200 nm, 1 nA corresponds to ~0.8 A cm^{-2}), which have also been observed in other SECCM and ultramicroelectrode studies. (*30*, *31*) The current density under Ar indicates that H_2O is the principal proton donor for H_2 evolution in the SECCM experiments. Under CO_2, diffusion of CO_2 into the nanodroplet enables a very high flux to the electrode surface. [Modeling this transport mechanism indicated that the CO_2 mass transport limit is ~3×10^{-13} mol s^{-1} (fig. S13)]. The current densities for both H_2O reduction and CO_2 reduction in SECCM were much larger than would be expected based on bulk electrolysis in HCO_3^- electrolyte at comparable potential. These results suggest that Au cathodes are rapidly and extensively poisoned by CO produced by CO_2 reduction and impurity adsorption in bulk experiments, masking the activity of uninhibited Au surfaces in cathodic reactions.

The width of the regions with increased current at the GB surface terminations in Fig. 3 was between 0.5 and 4 μm. To assess the structural perturbations associated with this catalytic footprint, high-resolution (HR) EBSD patterns were collected across individual GBs. The patterns were subsequently subjected to cross-correlative pattern analysis to measure small shifts in lattice parameters, which enabled quantification of the strain in the vicinity of the GB relative to distal regions (Fig. 4) (full maps in fig. S9) (*32*–*37*). For the GB corresponding to the heat map in Fig. 3E, the lattice strain monotonically increased with proximity to the GB, which is consistent with earlier studies showing that the structural perturbation in the vicinity of GBs was on the order of tens of micrometers (*38*). However, we found that the sharpest inflections in the lattice microstrain occurred in a ~2-μm width around the GB region (Fig. 4, A to D), which is comparable to the catalytic footprint.

This strain reflected the local "pile-up," or concentration, of dislocations in the GB region, as detailed in previous efforts to quantify dislocations at GB regions (*38*–*41*). In comparison, the strain profile induced by the Σ3 GB did not exhibit a noticeable slope in either grain, and only weak inflections in lattice microstrain were observed proximate to the Σ3 GB (Fig. 4, E to H), reflecting a lower relative concentration of dislocations in the GB region. The contrast in the strain profiles of the 17° GB and Σ3 GB tracks with the attenuated enhancement in CO_2 reduction observed for the Σ3 GB. It is important to note that the concentration of dislocations near a GB cannot be deduced from the GB geometry directly and is strongly dependent on the sample history. In addition, the dislocation density can vary substantially along a single GB. (*38*, *42*)

The combination of SECCM measurements and HR-EBSD strain mapping demonstrates that GB surface terminations selectively increased CO_2 reduction activity over a length scale determined by the GB strain field, which reflects the local density of dislocations. The GB-activity correlation observed in bulk electrolyses is a direct result of the activity of GB surface terminations. Because the catalytic footprint of the GB surface terminations can be quite large (on the scale of micrometers), the effect of increasing the total GB concentration was expected to saturate as the GB density increased, which was evident in Fig. 2G. In other words, the benefit of adding more GBs decreased as the grain size got smaller because the dislocation density saturated when

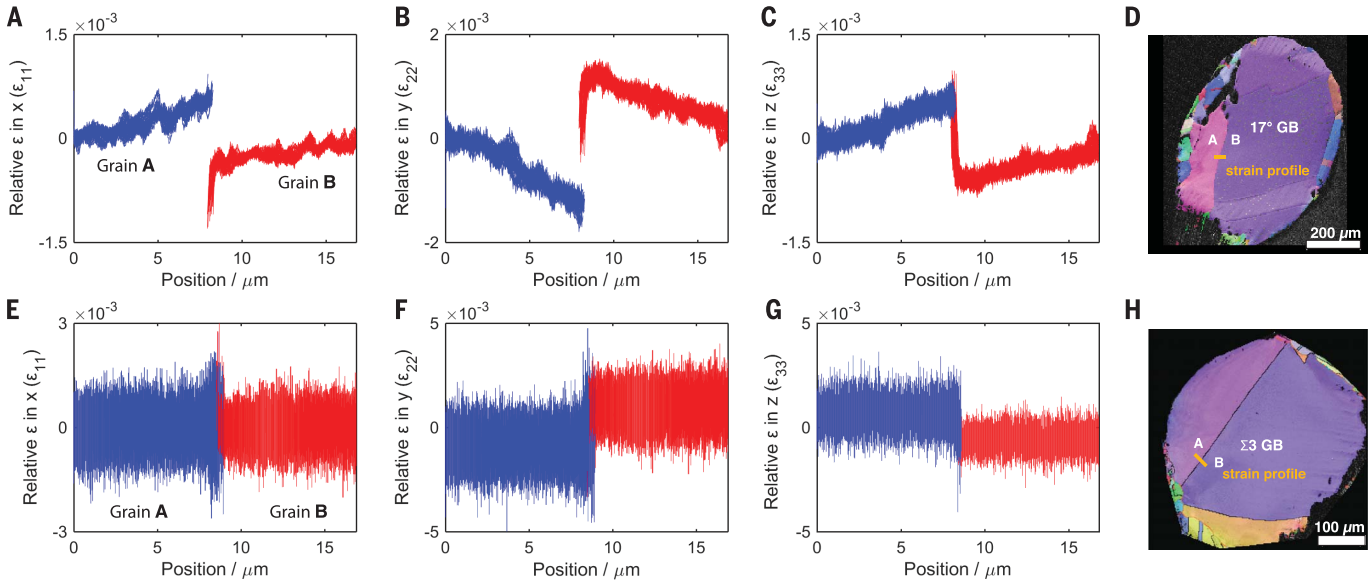

Fig. 4. HR-EBSD microstrain profiles of non-CSL and Σ3 GBs probed in Fig. 3. Each color denotes a microstrain profile for a single grain, each measured relative to a reference pixel at positions = 0 μm (for left, blue grain) and 16.8 μm (red, right grain). (**A** to **D**) Left to right: lattice microstrain profiles showing lattice distortion in the *x*, *y*, and *z* axes and the EBSD orientation map showing the strain map region for the 17° GB interrogated in Fig. 3, B to E. A large inflection is observed at ~8 μm, the location of the GB. (**E** to **H**) Left to right: lattice microstrain profiles in the *x*, *y*, and *z* axes and EBSD orientation map showing the strain map for the Σ3 GB interrogated in Fig. 3, G and H.

the strain fields of the GB surface terminations overlapped. This finding parallels a long-standing observation in metallurgy, in which attempts to strengthen materials by simply decreasing grain size yields progressively diminishing returns (*43*). The saturation observed here contrasts with the linear GB-activity relationships we previously observed over a large GB density range for NP catalysts. GBs in NPs typically have much narrower strain fields that consequently have little overlap, even at high GB density. (*44*, *45*)

The identification of GB-stabilized dislocations as structural elements that increase local activity implies that procedures that increase dislocation density should improve the activity of bulk samples. Mechanical treatments are frequently used in metallurgy to harden metals by inducing the formation of dislocation clusters and new GBs (*46*, *47*). Thus, we investigated the ability of mechanical treatments to restore CO_2 reduction activity to electrodes whose GB density had been reduced by annealing. Two strain-hardening treatments were applied to an Ann. 500 sample: hammering by hand on a small anvil, and a more intensive cold-rolling procedure (*48*, *49*). We chose mechanical treatment as a method to alter grain structure to minimize electrode roughening.

SEM images (fig. S10) indicate that the mechanically treated samples exhibit no long-range mesostructuring. Measurement of the electrodes' electrochemical surface area indicates roughness factors of ~1 and ~1.2 for the hammered and cold-rolled sample, respectively (table S2). By EBSD (fig. S11), a decrease in grain size was observed with deformation, concomitant with changes in surface orientation, while dislocation clusters were observed to begin forming new GBs. Pb UPD voltammograms (fig. S11) indicated that the parent Ann. 500 and the hammered sample consisted predominantly of Au(111) surface facets, whereas the cold-rolled sample exhibited a high proportion of Au(110), in addition to a minor population of Au(111).

The increased defect density in the mechanically treated samples translated into substantial increases in CO_2 reduction activity. At −0.4 V versus RHE, j_{CO} for the hammered foil was higher by a factor of ~2.3 than the parent Ann. 500 foil. The cold-rolled sample, which was even more defect rich, showed a j_{CO} higher by a factor of ~3.9 than Ann. 500 and was ~50% more active than un-annealed Poly-Au. (fig. S11). In contrast, j_{H2} decreased by ~30 and ~40% for the cold-worked and hammered samples, respectively. Given the large differences in faceting observed between the hammered and cold-rolled samples, these results demonstrated that the defects introduced by mechanical treatment were responsible for selectively increasing CO_2 reduction activity. Despite possessing no mesostructuring to increase local pH, or hydrophobic backing to enhance CO_2 transport, the j_{CO} of cold-rolled sample was within a factor of 2 of the highest surface area–normalized activity that has been previously reported for a nanostructured Au electrode (*50*).

We envision two possible explanations for the increase in CO_2 reduction activity at regions with high dislocation densities. Lattice strain at the surface induced by dislocations could alter the binding energies for CO_2 reduction intermediates in a way that reduces the overall barrier (*51*, *52*). Alternatively, dislocation surface terminations may create high step densities that are more active than terraces (*53*, *54*). Resolving these and other possible contributions will require atomic-level structural information under operating conditions. Although there are many possible strategies for creating strained or stepped surfaces, surface restructuring during catalysis can cause rapid relaxation of high-energy surfaces. High-energy surface structures that arise from bulk defects are likely to be more resistant to such degradation. The dislocation density of a polycrystalline material is determined not just by the GB density but by the GB character distribution as well (*1*, *55*). Our results therefore motivate the use of GB engineering to control these properties in heterogeneous catalysts.

REFERENCES AND NOTES

1. T. Watanabe, *J. Mater. Sci.* **46**, 4095–4115 (2011).
2. A. Rollett, G. Gottstein, L. Shvindlerman, D. Molodov, *Z. Metallk.* **95**, 226–229 (2004).
3. Y. Chen, C. W. Li, M. W. Kanan, *J. Am. Chem. Soc.* **134**, 19969–19972 (2012).
4. C. W. Li, J. Ciston, M. W. Kanan, *Nature* **508**, 504–507 (2014).
5. A. Verdaguer-Casadevall *et al.*, *J. Am. Chem. Soc.* **137**, 9808–9811 (2015).
6. X. Feng, K. Jiang, S. Fan, M. W. Kanan, *J. Am. Chem. Soc.* **137**, 4606–4609 (2015).
7. X. Feng, K. Jiang, S. Fan, M. W. Kanan, *ACS Cent. Sci.* **2**, 169–174 (2016).
8. S. Choi *et al.*, *Chem. Cat. Chem.* **7**, 2077–2084 (2015).
9. X. Sun, K. Jiang, N. Zhang, S. Guo, X. Huang, *ACS Nano* **9**, 7634–7640 (2015).
10. X. Huang *et al.*, *Nano Lett.* **14**, 3887–3894 (2014).
11. C. Wang *et al.*, *Nano Lett.* **16**, 5669–5674 (2016).
12. B. D. Aaronson *et al.*, *J. Am. Chem. Soc.* **135**, 3873–3880 (2013).
13. J. C. Byers, A. G. Güell, P. R. Unwin, *J. Am. Chem. Soc.* **136**, 11252–11255 (2014).
14. N. Ebejer *et al.*, *Annu. Rev. Anal. Chem.* **6**, 329–351 (2013).
15. A. G. Güell *et al.*, *Nano Lett.* **14**, 220–224 (2014).
16. D. Dingley, V. Randle, *J. Mater. Sci.* **27**, 4545–4566 (1992).
17. F. Humphreys, *J. Mater. Sci.* **36**, 3833–3854 (2001).
18. F. Humphreys, *Scr. Mater.* **51**, 771–776 (2004).
19. G. Rohrer *et al.*, *Mater. Sci. Technol.* **26**, 661–669 (2010).
20. See the supplementary materials.
21. J. Hernández, J. Solla-Gullón, E. Herrero, *J. Electroanal. Chem.* **574**, 185–196 (2004).
22. J. Cho, H. Ha, K. Oh, *Metall. Mater. Trans. A Phys. Metall. Mater. Sci.* **36**, 3415–3425 (2005).
23. A. Wuttig, Y. Surendranath, *ACS Catal.* **5**, 4479–4484 (2015).
24. A. S. Hall, Y. Yoon, A. Wuttig, Y. Surendranath, *J. Am. Chem. Soc.* **137**, 14834–14837 (2015).
25. C. H. Chen, K. E. Meadows, A. Cuharuc, S. C. Lai, P. R. Unwin, *Phys. Chem. Chem. Phys.* **16**, 18545–18552 (2014).
26. C. H. Chen *et al.*, *Anal. Chem.* **87**, 5782–5789 (2015).
27. A. Hassel, M. Seo, *Electrochim. Acta* **44**, 3769–3777 (1999).
28. J. Perez, E. Gonzalez, H. Villullas, *J. Phys. Chem. B* **102**, 10931–10935 (1998).
29. A. Wuttig, M. Yaguchi, K. Motobayashi, M. Osawa, Y. Surendranath, *Proc. Natl. Acad. Sci. U.S.A.* **113**, E4585–E4593 (2016).
30. C. L. Bentley *et al.*, *Chem. Sci.* **8**, 6583–6593 (2017).
31. M. Tavares, S. Machado, L. Mazo, *Electrochim. Acta* **46**, 4359–4369 (2001).
32. S. Villert, C. Maurice, C. Wyon, R. Fortunier, *J. Microsc.* **233**, 290–301 (2009).
33. M. D. Vaudin *et al.*, *Ultramicroscopy* **148**, 94–104 (2015).
34. M. Calcagnotto, D. Ponge, E. Demir, D. Raabe, *Mater. Sci. Eng. A* **527**, 2738–2746 (2010).
35. K. Troost, P. Vandersluis, D. Gravesteijn, *Appl. Phys. Lett.* **62**, 1110–1112 (1993).
36. Y. Guo, T. Britton, A. Wilkinson, *Acta Mater.* **76**, 1–12 (2014).
37. A. Wilkinson, D. Randman, *Philos. Mag.* **90**, 1159–1177 (2010).
38. J. Jiang, T. Britton, A. Wilkinson, *Acta Mater.* **61**, 7227–7239 (2013).
39. P. Littlewood, T. Britton, A. Wilkinson, *Acta Mater.* **59**, 6489–6500 (2011).
40. S. Sun, B. Adams, W. King, *Philos. Mag. A* **80**, 9–25 (2000).
41. J. Hu, S. Chang, F. Chen, J. Kai, *Mater. Chem. Phys.* **74**, 313–319 (2002).
42. H. Abdolvand, A. J. Wilkinson, *Int. J. Plast.* **84**, 160–182 (2016).
43. E. Nes, *Prog. Mater. Sci.* **41**, 129–193 (1997).
44. T. Radetic, F. Lançon, U. Dahmen, *Phys. Rev. Lett.* **89**, 085502 (2002).
45. A. Ulvestad, J. N. Clark, R. Harder, I. K. Robinson, O. G. Shpyrko, *Nano Lett.* **15**, 4066–4070 (2015).
46. R. Valiev, A. Korznikov, R. Mulyukov, *Mater. Sci. Eng. A* **168**, 141–148 (1993).
47. V. Stolyarov, Y. Zhu, I. Alexandrov, T. Lowe, R. Valiev, *Mater. Sci. Eng. A* **343**, 43–50 (2003).
48. R. Ueji, N. Tsuji, Y. Minamino, Y. Koizumi, *Acta Mater.* **50**, 4177–4189 (2002).
49. E. J. Gwak, J. Y. Kim, *Nano Lett.* **16**, 2497–2502 (2016).
50. M. Liu *et al.*, *Nature* **537**, 382–386 (2016).
51. M. Gsell, P. Jakob, D. Menzel, *Science* **280**, 717–720 (1998).
52. M. Mavrikakis, B. Hammer, J. Nørskov, *Phys. Rev. Lett.* **81**, 2819–2822 (1998).
53. J. V. Barth, H. Brune, G. Ertl, R. J. Behm, *Phys. Rev. B Condens. Matter* **42**, 9307–9318 (1990).
54. H. A. Hansen, J. B. Varley, A. A. Peterson, J. K. Nørskov, *J. Phys. Chem. Lett.* **4**, 388–392 (2013).
55. S. Kobayashi, S. Tsurekawa, T. Watanabe, *Beilstein J. Nanotechnol.* **7**, 1829–1849 (2016).

ACKNOWLEDGMENTS

This research was supported by NSF (CHE-1565945) and the Air Force Office of Scientific Research Multidisciplinary Research Program of the University Research Initiative (FA9550-14-1-0003). R.M. gratefully acknowledges NSF for a predoctoral fellowship. We thank C. Spence (Gatan, Inc.) for preparation of Ar ion milled samples. EBSD was performed at the Stanford Nano Shared Facilities (SNSF), which is supported by NSF under award ECCS-1542152. All data are reported in the main text and the supplementary materials.

SUPPLEMENTARY MATERIALS

www.sciencemag.org/content/358/6367/1187/suppl/DC1
Materials and Methods
Figs. S1 to S13
Tables S1 and S2
References

12 July 2017; accepted 23 October 2017
10.1126/science.aao3691

Selective increase in CO_2 electroreduction activity at grain-boundary surface terminations

Ruperto G. Mariano, Kim McKelvey, Henry S. White and Matthew W. Kanan

Science **358** (6367), 1187-1192.
DOI: 10.1126/science.aao3691

Going with the grain boundaries

Bulk defects in a metal, such as grain boundaries, can create regions of increased strain at its surface that could affect its catalytic activity. Mariano *et al.* studied the electroreduction of CO_2 to CO on polycrystalline gold films, a reaction that competes with H_2 evolution. By annealing the films to create larger grains, they could change the types and distribution of grain boundaries at the surface. Scanning electrochemical cell microscopy revealed that the dislocation density correlated with CO_2 electroreduction activity, but such defects had no effect on H_2 evolution.

Science, this issue p. 1187